

UC San Diego

UC San Diego Previously Published Works

Title

Microscale Concert Hall Acoustics to Produce Uniform Ultrasound Stimulation for Targeted Sonogenetics in hsTRPA1-Transfected Cells

Permalink

<https://escholarship.org/uc/item/8jd69469>

Journal

Advanced NanoBiomed Research, 2(5)

ISSN

2699-9307

Authors

Vasan, Aditya
Allein, Florian
Duque, Marc
et al.

Publication Date

2022-05-01

DOI

10.1002/anbr.202100135

Peer reviewed

Microscale Concert Hall Acoustics to Produce Uniform Ultrasound Stimulation for Targeted Sonogenetics in *hsTRPA1*-Transfected Cells

Aditya Vasan, Florian Allein, Marc Duque, Uri Magaram, Nicholas Boechler, Sreekanth H. Chalasani, and James Friend*

Ultrasound neuromodulation has rapidly developed over the past decade, a consequence of the discovery of strain-sensitive structures in the membrane and organelles of cells extending into the brain, heart, and other organs. A key limitation to its use in the brain is the formation of standing waves within the skull. In standing acoustic waves, the maximum ultrasound intensity spatially varies from near zero to double the mean in one-half of a wavelength, and has led to localized tissue damage and disruption of normal brain function while attempting to evoke a broader response. This phenomenon also produces a large spatial variation in the actual ultrasound exposure in tissue, leading to heterogeneous results. One approach to overcome this limitation is presented here: transducer-mounted diffusers that result in spatiotemporally incoherent ultrasound. It is shown through experiment and analysis that adding a diffuser to the transducer leads to a twofold increase in ultrasound responsiveness of transient receptor potential ankyrin 1 (*TRPA1*)-transfected human embryonic kidney cells. Furthermore, it is shown that the diffuser produces a uniform spatial distribution of pressure within the rodent skull. The approach offers uniform ultrasound delivery into irregular cavities for sonogenetics.

1. Introduction

Sound diffusers have been applied to concert hall acoustics since the 1800s, when ornamentation along the walls or concave ceilings were used to introduce greater binaural dissimilarity.^[1] Evolution of concert hall architecture eventually led to the development of the Schröder diffuser, arguably the first practical technique to disperse sound in a predictable manner. In the 1970s, Schröder proposed the phase grating diffuser,^[1,2] a method to artificially create diffuse reflection, with recent improvements to the design.^[3] Composed of regular wells of different depths, these structures are governed by a 2D pseudostochastic sequence. In the typical configuration, waves incident on this structure undergo phase shifts corresponding to the depth of the wells through which they travel. The structure then scatters sound rather than reflecting it, depending on


the magnitude of these phase shifts. This method has been widely adopted in architectural acoustics, where sound absorption—the only feasible alternative—is undesirable. This method has also been applied to ultrasound imaging^[4] and microparticle separation^[5] where sound absorption is likewise difficult. More recently, the principle of applying phase shifts to a coherent ultrasound field has led to the development of acoustic holography.^[6,7] This novel approach has enabled the generation of customized amplitude profiles based on the location and shape of the target region but has not yet been used to enable the creation of spatiotemporally incoherent fields within an enclosed cavity.

Ultrasound transducers have been used in neurological applications for imaging tissue,^[8] disrupting blood–brain barriers,^[9] invasive^[10] and noninvasive neuromodulation,^[11] and thrombolysis.^[12] In these cases, ultrasound is typically focused at a certain depth defined by a phased array of transducers^[13] or an acoustic lens formed by a concave surface at the exit face of the transducer.^[14] A fundamental limitation of these approaches is the formation of standing waves due to resonant reflections within the skull cavity formed by the relatively high impedance of the skull's cortical bone compared to the tissue of the brain, and thus regions of either extremely high intensity or zero intensity at

A. Vasan, J. Friend
Medically Advanced Devices Laboratory
Department of Mechanical and Aerospace Engineering
Jacobs School of Engineering and Department of Surgery
School of Medicine
University of California San Diego
La Jolla, CA 92093, USA
E-mail: jfriend@ucsd.edu

F. Allein, N. Boechler
Department of Mechanical and Aerospace Engineering
University of California San Diego
La Jolla, CA 92093, USA

M. Duque, U. Magaram, S. H. Chalasani
Molecular Neurobiology Laboratory
The Salk Institute for Biological Studies
La Jolla, CA 92037, USA

 The ORCID identification number(s) for the author(s) of this article can be found under <https://doi.org/10.1002/anbr.202100135>.

© 2022 The Authors. Advanced NanoBiomed Research published by Wiley-VCH GmbH. This is an open access article under the terms of the Creative Commons Attribution License, which permits use, distribution and reproduction in any medium, provided the original work is properly cited.

DOI: 10.1002/anbr.202100135

every one-half of an acoustic wavelength.^[15] The presence of these local maxima may lead to unintended bioeffects in tissues when applied to neuromodulation,^[16] including heating or even tissue damage from cavitation.^[17] Such adverse effects in tissue have been reported during ultrasound-driven thrombolysis and blood–brain barrier disruption.^[18,19] Additionally, commonly used transducer materials such as lead zirconate titanate (PZT) also have limitations in high power applications at frequencies above ≈ 1 MHz, producing losses, hysteresis, and internal (ohmic) heating as current passes through elemental lead present at the morphological grain boundary,^[20] which limits the use of broadband stochastic signal generation for reducing the impact of standing wave generation. One approach to overcome these limitations is to build resonant devices using loss-free, single-crystal piezoelectric material to generate single-frequency ultrasound output in the 1–10 MHz range that has an attached diffuser and is thus capable of delivering a spatiotemporally diffuse ultrasound field for various applications, including sonogenetics.

Sonogenetics relies on genetically engineering cells to be more sensitive to mechanical stimuli using membrane-bound proteins.^[21,22] This technique eliminates the need for focused ultrasound by ensuring that targeted neural circuits are the only ones that will respond to an ultrasound stimulus. Currently, the method of transfection uses adeno-associated virus (AAV) delivered by syringe, an invasive method, though there is reason to believe minimally invasive AAV transfection techniques are forthcoming.^[23,24] Recent work has revealed that one protein in particular, human transient receptor potential A1 (hTRPA1), produces ultrasound-evoked responses in several cell types.^[22] This response is due to deformation and consequent stretching of the cell membrane from exposure to ultrasound that, in turn, leads to a change in the membrane capacitance between a chemically induced potential difference from inside to outside the cell. This produces a current sufficient to cause hTRPA1 responses.^[25] One limitation of sonogenetics is that existing transducers producing planar or focused ultrasound, typically at a single frequency, are unsuitable. Furthermore, in many applications, the transducer must be small to avoid affecting animal behavior, which excludes phased array based approaches. Transducers that can be attached to freely moving mice enable the study of neural circuits in their native state, without the

confounding effects of anesthesia as reported in past studies.^[26,27] Unfortunately, no small broadband transducers exist^[28,29] that might facilitate the generation of spatiotemporally random ultrasound noise from a similarly random input signal at sufficient power for sonogenetics. Moreover, commonly used animal models like rodents have small heads with a typical mass of 3–4 g,^[30] less than half the mass of all commercially available or research-based^[31] power ultrasound transducers known to the authors.

The effective implementation of sonogenetics requires a very different transducer design. It must reduce interference between the radiated and reflected ultrasound, produce diffuse and uniform ultrasound throughout the region, and transduce sufficient power to produce over 0.4 MPa acoustic pressure in tissue, all while remaining sufficiently small and light enough to attach to the head of a live, freely moving mouse. This would enable the study of neural circuits in their more native state. In addition, these devices also have to avoid generating electromagnetic signals and localized temperature changes. If left to appear, electromagnetic and thermal phenomena may conflate with the effects of ultrasound on the cells in sonogenetics experiments, reducing one's confidence in ultrasound's contribution to the observations.

We have overcome the limitations of existing transducers by incorporating a machined diffuser on the transducer face in order to produce spatiotemporally incoherent MHz-order ultrasound (**Figure 1**). Diffusers are typically used in reducing coherent reflected sound—echoes—and their use on the sound generator itself has not been reported to the knowledge of the authors. A diffuser is ideally suited for sonogenetics as it nearly losslessly reduces the presence of regions of either high or low intensity within an enclosed cavity, in both in vitro assays and within the rodent skull for longer term applications. First, we discuss the design of the diffuser and validate its performance using numerical simulations. We then address the challenge of fabrication of a complex 3D structure at submillimeter scales, as conventional photolithography, 3D printing, and classic machining techniques are unsuitable for this task. Next, we characterize a device which has been coupled to a lithium niobate transducer operating in the thickness mode.^[32] We then present an application of the Schröder diffuser to screen for ultrasound-sensitive ion channels in human embryonic kidney (HEK293)

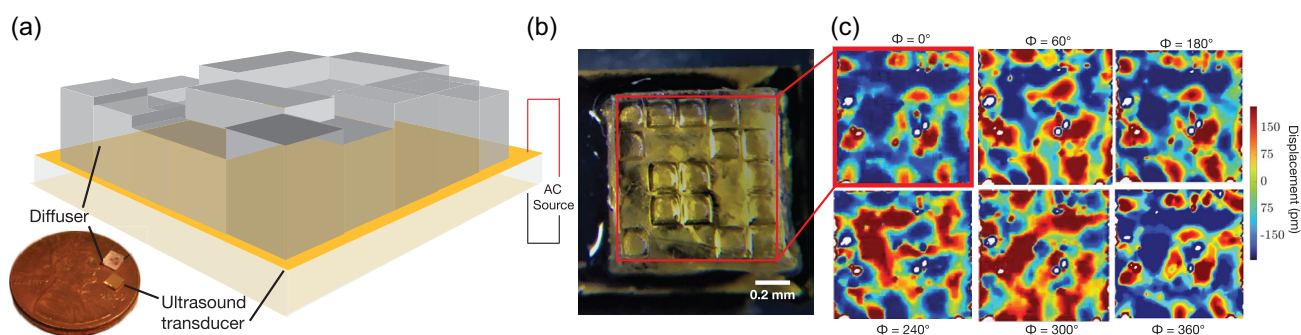


Figure 1. a) A diffuser design based on Schröder's method of quadratic-residue sequences to determine well depth. The wells were machined in glass using a KrF excimer laser system with a custom metal mask to restrict beam width. The machined depth of the pillars is up to 309 μm . b) The glass diffuser block was then c) bonded to a transducer operating in the thickness mode at 7 MHz using an ultraviolet light-curable epoxy. (c) A scanning laser Doppler vibrometer image of the diffuser face in the time domain shows phase differences corresponding to pillar heights (normalized autocorrelation > 0.73).

cells in vitro for the purposes of identifying and isolating targets for sonogenetics in freely moving mice. Finally, we verify the presence of nearly equivalent acoustic pressures across two deep brain regions in an ex vivo model.

2. Results

The design of the Schröder diffuser is based on quadratic-residue sequences defined by $s_n = n^2$, where n^2 is the least non-negative remainder mod N , with N always an odd prime. One of the properties of this number sequence relevant to the design of an optimum diffuser is that both the Fourier transform of the exponential sequence $r_n = \exp(i2\pi s_n/N)$ and by extension the scattered wave produced by it have a constant magnitude^[1,33] $|R_m|$ such that

$$|R_m|^2 = \left| \frac{1}{N} \sum_{n=1}^N r_n e^{-\frac{2\pi i m n}{N}} \right|^2 = \frac{1}{N} \quad (1)$$

where $\iota = \sqrt{-1}$.

We may then use this to define the wells' depths, $d(x_n, y_n)$, corresponding to the number sequence. In one dimension, the depth of the n th well is given by^[34]

$$L_n = \frac{\pi c n^2 (\text{mod } N)}{N \omega_r} \quad (2)$$

where ω_r is the design frequency, N is a prime number, and c is the speed of sound in the medium. Extending the concept of a diffuser defined per the above numerical sequence to two dimensions involves replacing n^2 in the above formula with $n^2 + m^2$, where m represents the number of wells in the second dimension. A representative image of a diffuser fabricated using a 2D sequence is shown in Figure 1.

While a 1D diffuser creates a uniform 2D pressure field, a 2D diffuser with varying well depths creates a uniform 3D pressure field. Ultrasound neuromodulation typically relies on frequencies in the 1–10 MHz range^[35] and this requires submillimeter well depths as defined by Equation (2). Although structures based on the quadratic-residue sequence have been achieved at the macroscale in two dimensions and at the microscale in one dimension,^[5] it has not been achieved in 2D structures on the micron to submillimeter scale due to the lack of established fabrication techniques for these dimensions.^[36] Conventional photolithography is good for creating patterns that have the same depth or, at most, a few different depths. It becomes challenging when features of varying depths are desired because multiple photolithography and etching steps are required. Alternate approaches, including 3D or two-photon printing methods, are unable to produce acoustically low-loss structures with sufficient dimensional accuracy at these scales. We sought to address these limitations by using an excimer laser to machine submillimeter pillars of varying heights in glass in two dimensions. Significant phase correlation (normalized autocorrelation >0.73) with the machined geometry is apparent from a time-domain laser Doppler vibrometry (LDV; see Experimental Section) scan shown in Figure 1. The transducer was driven at its resonance frequency with a sinusoidal input power range of 0.5–2 W and a peak

pressure output of 0.6 MPa as measured with a fiber optic hydrophone.^[37]

The benefit of using the diffuser was considered using finite element analysis (COMSOL 5.5, Comsol Inc., Los Angeles, CA, USA). The domain was chosen to mimic an experimental setup used for identifying ultrasound-sensitive ion channels in an in vitro setup. This consists of an inverted fluorescence microscope with a custom perfusion chamber to house a coverslip and transducer. The simulation domain is illustrated in Figure 2 and specific dimensions of the domain and simulation parameters are described in the Experimental Section. Due to computational constraints, the simulation was modeled in two dimensions with 17 wells instead of the full 25-well system. The transducer and the diffuser assembly were fixed at the bottom of the domain. A custom perfusion chamber that contains a slot for a coverslip was mounted over the ultrasound source. The transducer was coupled to the coverslip through water and there was a layer of media above the coverslip. The walls were defined to be rigid boundaries with an acoustic impedance $Z_i = \infty$ such that the normal derivative of the total acoustic pressure $\frac{\partial p}{\partial n} = 0$. The diffuser consists of 17 elements, the heights of which were calculated from Equation (2). The coverslip serves as a solid boundary and allows the evaluation of the acoustic field in the closed domain below and the open domain above it, corresponding to the different boundary conditions assigned to the model.

The time variation of the pressure field with and without the diffuser was evaluated (Video S1 and S2, Supporting Information). Several points in the fluid domain were chosen and the time evolution of the pressure field for the two cases was compared using the techniques described in the Experimental Section. A 2D autocorrelation was calculated in order to determine if there were any locations within the domain with coherence (echoes) or localized increases or decreases (constructive and destructive interference) in ultrasound intensity. Spatial and temporal patterns that form over the duration of the stimulus are represented by a 2D autocorrelation in Figure 2. It is evident that there is both spatial and temporal periodicity with the transducer alone (Figure 2a and Video S1, Supporting Information) that is greatly reduced when the diffuser is introduced (Figure 2b and Video S2, Supporting Information). Videos of the sample autocorrelation in the domain over the stimulus duration are presented in Video S3 and S4, Supporting Information and show that there is greater autocorrelation over the duration of the stimulus without the diffuser (Video S3, Supporting Information). This indicates that the ultrasound field with the diffuser is temporally aperiodic.

For the purpose of quantifying any changes to the diffraction at 7 MHz through the inclusion of the diffuser, an isofrequency contour plot of the simulated data is provided in Figure 3a without and Figure 3b with the diffuser. Without the diffuser, wave vectors are only present in the vicinity of $k_x = 0$, along the direction of propagation of the pressure wave in the medium: the Y axis. The angular spread is 20° on either side of the direction of propagation without the diffuser. Particularly, the majority of the wave can be seen to be propagating along the Y axis, with significant sidelobes immediately to the left and right and much smaller sidelobes slightly farther away. Including the diffuser

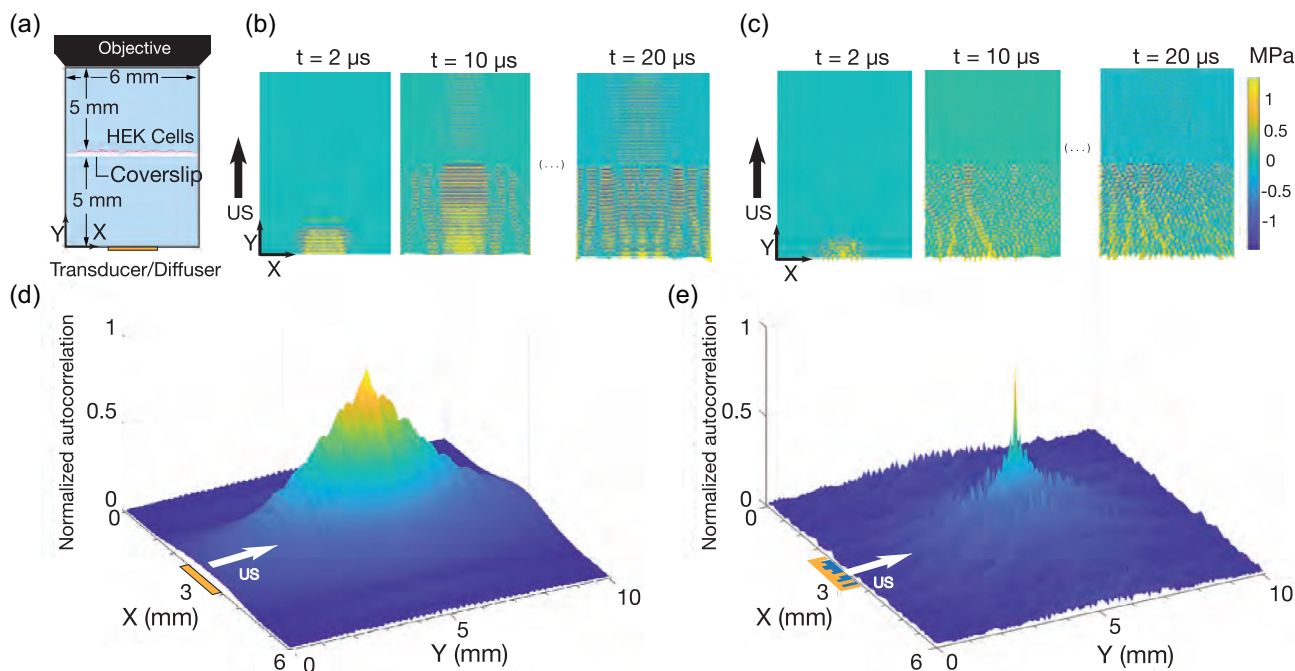


Figure 2. 2D instantaneous pressure profile for the a) domain b) without and c) with the diffuser. Human embryonic kidney (HEK) cells were placed in the middle of the (light blue) fluid domain with an objective lens for an inverted microscope at top. The pressure field was generated by defining a sinusoidal pressure displacement to the transducer face, located at the bottom of the domain. Pressure maps were extracted from the results in $1 \mu\text{s}$ time steps over grid points specified within the domain. A 2D autocorrelation was performed on this grid over time; each X,Y point plotted from the d,e) results of the autocorrelation corresponds to a single point in the (a) domain. Spatial and temporal periodicity was observed through the existence of a large value of autocorrelation over the domain (d) without the diffuser. e) With the diffuser, however, the autocorrelation was much smaller for most of the domain.

produces wave vectors beyond the main direction of propagation (Figure 3b), with significant components oriented along directions from the Y axis (along k_x) to the X axis (along k_y). The previously significant sidelobes remain significant, but are augmented by wave propagation beyond 45° in the XY plane. This indicates strong diffraction from the face of the transducer when including the diffuser. The RMS pressure was calculated to determine the temporal and spatial distribution of pressure $10 \mu\text{m}$ above the coverslip, as shown in Figure 3c. The inclusion of the diffuser results in an even RMS pressure distribution along the coverslip, whereas the control case shows a fivefold variation of pressure across the coverslip face.

To verify the effects of the diffuser in vitro, we used an upright optical imaging setup including an immersion objective, a custom perfusion chamber, and the diffuser assembly. The diffuser assembly and the test setup are shown in Figure 4a; we used lithium niobate due to its relatively high coupling coefficient and zero hysteresis^[38] which implies no heating from the piezoelectric material itself. Human embryonic kidney (HEK293) cells expressing GCaMP6f^[39] were transfected with hsTRPA1. We compared fluorescence changes ($\frac{\Delta F}{F}$) for four cases, with and without the channel, without the diffuser assembly (transducer alone), and with the diffuser assembly. Representative GCaMP6f images of HEK293 cells transfected with hsTRPA1 are shown in Figure 4b and heat maps of fluorescence intensity with respect to time are presented in Figure 4c, with a clear increase in both the magnitude and number of cells being activated with the diffuser

assembly. Cells expressing hsTRPA1 and controls were tested at two different pressure amplitudes, 0.32 and 0.65 MPa, with the ambient pressure as the reference (zero) pressure. There was a consistent increase in fluorescence intensity with an increase in acoustic pressure for both the control and the hsTRPA1 condition, whether or not the diffuser was present. Including the diffuser increased the mean fluorescence amplitude by at least a factor of two for cells that had been infected with hsTRPA1 ($p < 0.0001$; Figure 4d).

We also tested the effects of ultrasound on mouse primary cortical neurons. Neurons were infected with adeno-associated viral (AAV) vectors to express hsTRPA1 and a genetically encoded calcium indicator, GCaMP6f,^[39] or a control with only the calcium indicator. We found that ultrasound triggered an increase in calcium uptake in both cases, with the hsTRPA1 neurons showing a greater number of activated cells in comparison to the control (Figure S2, Supporting Information). A video of real-time calcium response in hsTRPA1-expressing neurons is presented in Video S5, Supporting Information.

The uniform nature of the ultrasound field created by the diffuser was also verified ex vivo in a mouse skull while keeping as much of the mouse skull intact during preparation as possible (see Experimental Section). Pressure measurements were taken at two different locations as indicated in Figure 5 along the anterior–posterior axis, at the ventral surface of the pons and the ventral surface of the anterior olfactory bulb. With the diffuser, the pressure at both these locations was uniform, with

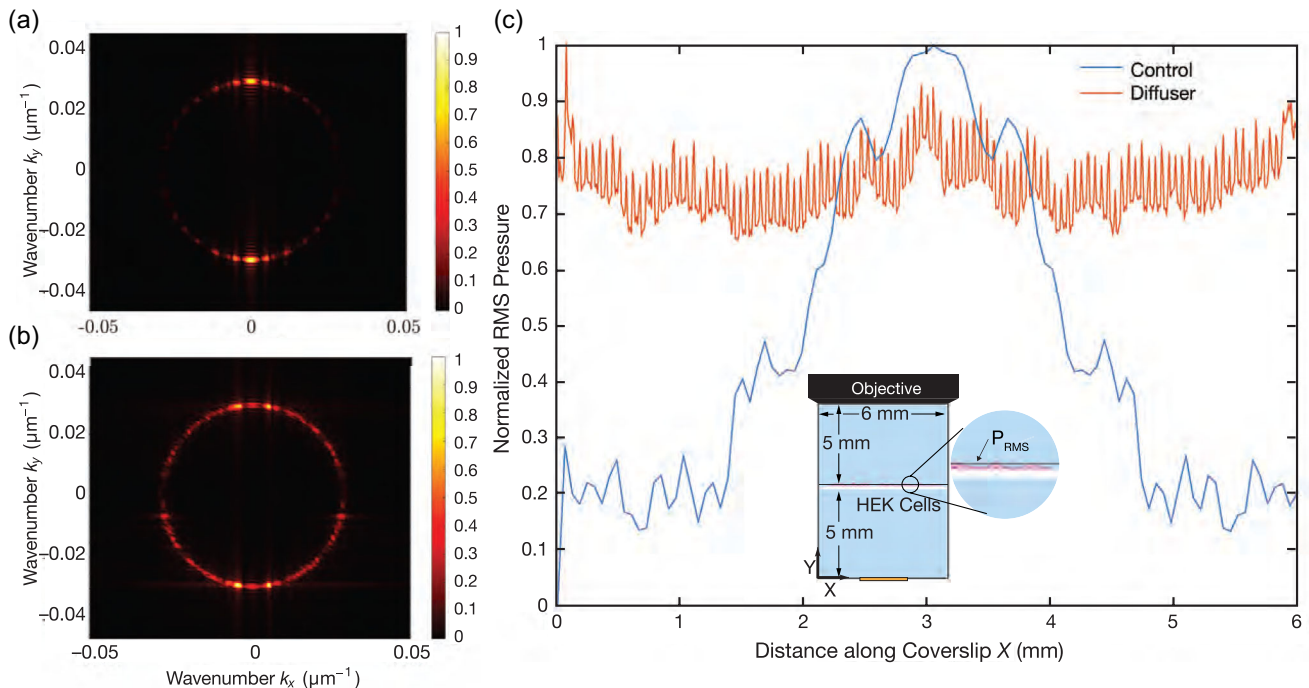


Figure 3. Calculated isofrequency contour at the driving frequency a) without and b) with the diffuser. The circular profile traced by both cases corresponds to the wave vector in water at the driving frequency. (a) Without the diffuser, most of the wave is isolated to propagation along the Y axis. Using (b) a diffuser with the transducer produced wave vectors spread around this circular profile, indicating a more uniform distribution of the ultrasound. Calculating (c) the normalized root mean square (RMS) pressure 10 μm above the coverslip (inset; halfway between the transducer and objective lens) indicates a smaller difference between the minimum and maximum RMS values (red) with the diffuser than (blue) without it. The diffuser produces a much more uniform pressure distribution across the coverslip plane.

minimal deviation between them and a uniform increase with input power to the transducer (Figure 5). However, the transducer alone produced diverging values of pressure at these positions, so much so that the pressure at the pons (triangle) exceeded the pressure at the anterior olfactory bulb (circle) by a factor of 3 at an input power of 3 W, yet fell below the hydrophone's minimum measurement value, 0.2 MPa, at the anterior olfactory bulb when using less than 1.25 W of power. By contrast, the diffuser had minimal deviation in pressure values at these locations, with pressure values ranging from 0.25 to 0.5 MPa at the ventral surface of both the pons and the anterior olfactory bulb. These brain regions were chosen not for their function, but because they were remote and would therefore be expected to exhibit standing-wave behavior with large variations in the acoustic pressure. Collectively, these results demonstrate that the diffuser is capable of delivering uniform ultrasound fields *in vivo* in comparison to the transducer alone, thus enabling sonogenetic studies across large brain regions.

3. Discussion

Existing non- and minimally invasive techniques to stimulate brain regions, such as transcranial magnetic stimulation and transcranial direct current stimulation, offer poor spatial resolution. This is a problem for precisely targeting brain regions that

have specific functions. Ultrasound-based stimulation enables targeting brain regions with submillimeter-scale accuracy. This precision can be achieved in different ways, either by using an array to focus ultrasound to a specific region^[40] or by using sonogenetics to engineer cells to locally be more sensitive to mechanical stimuli. The development of sonogenetics that started with the TRP4 channel has expanded to include a library of proteins that are sensitive to ultrasound stimuli at different ultrasound stimulation parameters. Examples include MSC,^[41] TREK,^[42] Piezo,^[43] and other TRP channels,^[44] all have been shown to be sensitive to ultrasound *in vitro*.

Still, a limitation with focused ultrasound is the alteration in the position and shape of the focal zone due to spatial variations in acoustic impedance.^[45] Sonogenetics is an attractive option because of the potential of having a toolkit of specific proteins that can be engineered to be sensitive to ultrasound stimuli at different frequencies or pressures. Current ultrasound transducers and how ultrasound interacts with the skull cavity are important limitations in translating sonogenetics into clinical practice. Standing waves in the skull cavity produce nodes and antinodes, each separated by one-half of the acoustic wavelength and responsible for pressure minima and maxima, respectively. This may lead to hemorrhage and heating in tissue^[18] as reported in past studies. One could attempt to overcome this issue by using broadband white noise to produce a spatiotemporally random acoustic field, but ultrasonic transducers are unable to

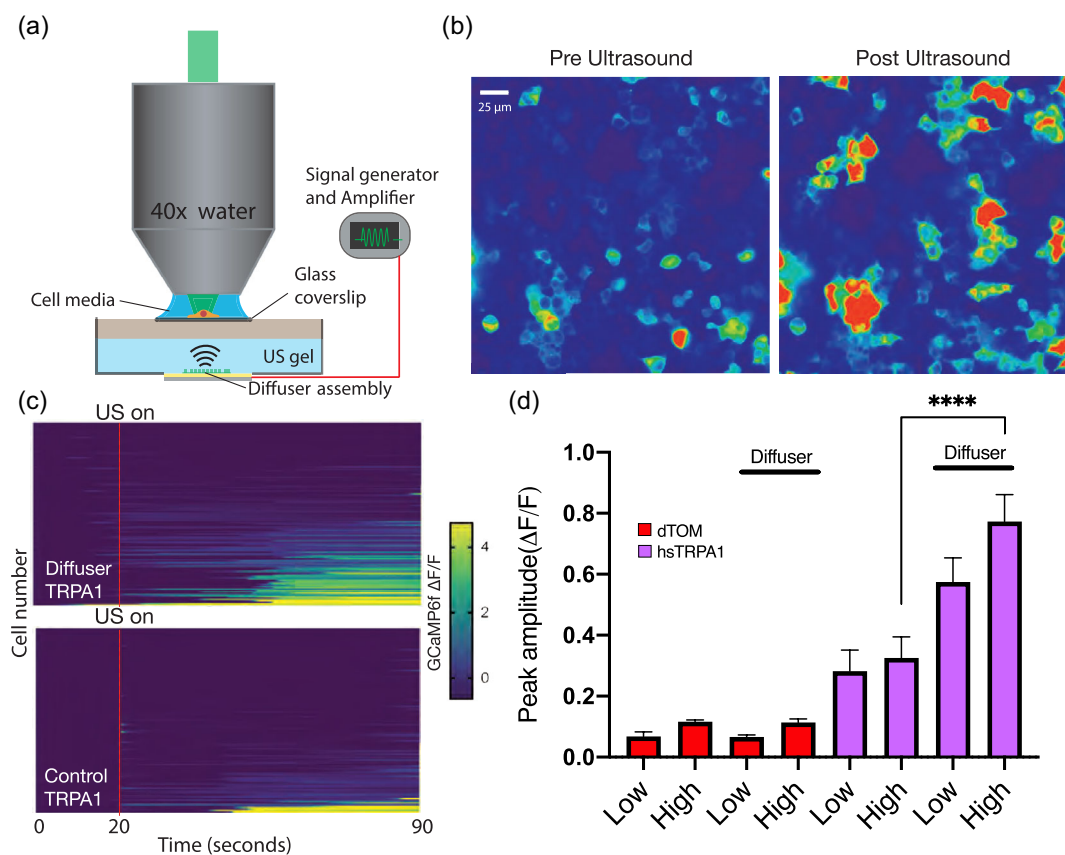


Figure 4. a) The experimental setup for confirming the utility of the diffuser in an in vitro setting consists of an upright epi-fluorescent microscope, an immersion objective, and a chamber that houses cells on a coverslip and the diffuser assembly. Standing wave components may exist between the transducer and the coverslip and between the coverslip and the immersion objective. The calcium concentration before and after ultrasound stimulation in the same field of view is b) shown for HEK cells expressing hS/TRPA1. Comparison of fluorescence changes as measured using GCaMP6f reporters with respect to time for two cases, c) without (control) and with the diffuser, shows an increase in both number and magnitude of cells being activated upon introduction of the diffuser. d) HEK cells expressing TRPA1 show a greater response to ultrasound stimuli with a diffuser present in comparison to both no diffuser and dTom-based (red fluorescent protein) controls. The magnitude of the response when the diffuser is used is significantly greater (over twice as high) than when the diffuser is not used ($n = 76 - 221$, **** $p < 0.0001$ by a Mann–Whitney test).

provide such noise at pressures sufficient to elicit cellular responses. Nevertheless, one should still consider the mechanical index for the ultrasound used in this study. It never exceeds 0.15, well below the U.S. Federal Drug Administration’s clinical safety threshold index of 1.9 without microbubbles,^[46,47] suggesting that we are unlikely to cause cavitation nor adverse heating effects. This result is supported by prior work with similar stimulus parameters^[22] where cell viability was maintained.

Designed via computational analysis and fabricated with an excimer laser, a microscale Schröder diffuser was devised to eliminate the spatiotemporally heterogeneous distribution of ultrasound by placing it upon the emitting transducer. The transducer alone was shown to produce standing waves in the absence of the diffuser. With the diffuser in place, autocorrelation of the ultrasound field quantifies the elimination of the standing waves and consequent suppression of antinodes associated with potential tissue damage. We verified the predictions of the simulation in vitro using HEK293 cells and neurons that were transfected with a sonogenetic candidate, hS/TRPA1.

Schröder’s original diffuser design was to be used for diffusion of reflected sound in the far field of the source, not the near field. There is a lengthy discussion regarding the distinction of these two regimes in Foote,^[48] but the essential feature is that near the transducer (in the near field) the acoustic field will be distributed differently than in the far field. If we take the most common definition for the distance of the boundary between the near and far fields from the transducer to be $z = a^2\lambda^{-1}$ where a is the lateral size of the transducer and λ is the wavelength, in our case the far field begins 120 mm away from the transducer. This is a far greater distance than the opposite side of the mouse skull, and so the entire system is in the near field. Beyond the difficult question of what defines “near field” versus “far field,” it has been observed in the literature across disciplines and scales that Schroeder’s diffusers designed for the far field also produce useful effects in the near field.^[3,49] There have been proposals, even by Schroeder, to modify the diffuser design to target the near field, but as far as we are aware, these have not gained traction due to fabrication difficulties and

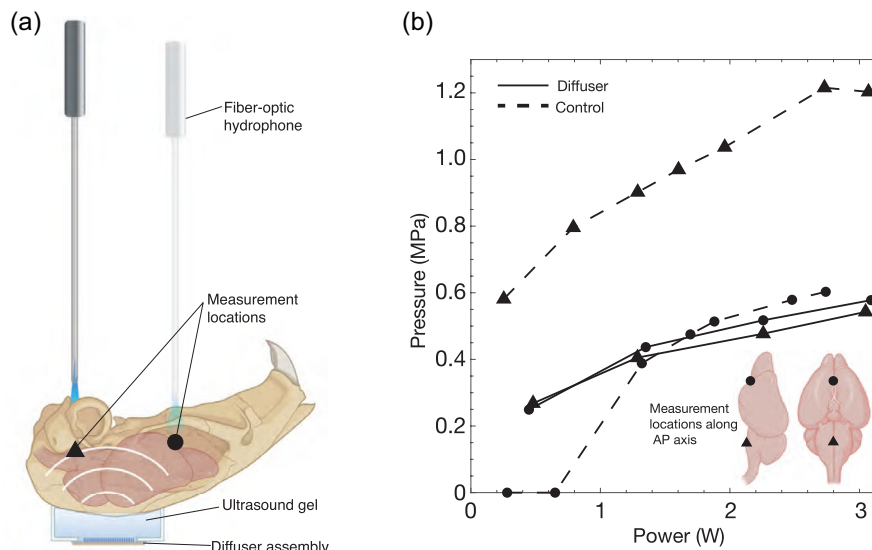


Figure 5. The pressure was measured using a) a fiber optic hydrophone at two different locations along the anterior–posterior axis: the ventral surface of the pons (triangle) and the ventral surface of the anterior olfactory bulb (circle). The measured pressure is b) uniform across different brain regions for different input powers above 0.2 MPa (minimum detectable pressure using our setup), indicating that the diffuser creates a uniform acoustic field within the skull cavity. This eliminates the influence of the cranial structure and ensures that only the brain regions that have been infected with hsTRPA1 will be sensitive to ultrasound stimuli. In comparison, the control case without the diffuser shows a threefold deviation in pressure values for the same input power for different brain regions along the AP axis.

modest improvements over the far field design. Our computational and experimental results in this and past studies appear to support this perspective. Specifically, in a microfluidics application,^[5] a “far field” Schröder diffuser was designed for cell manipulation, and yet it proved to be effective in the near field. Only with the current results is it apparent that mounting such a diffuser on the transducer itself—as near to the source as is physically possible—still produces an effective result.

Development of sonogenetics in larger animal models—such as primates—will require ultrasound transducers that are capable of delivering an acoustic field that is spatially and temporally incoherent, as we have shown with the diffuser assembly. This ensures that the pressure in different brain regions is uniform over the stimulus duration, thus eliminating the aberrations in the acoustic field due to the skull cavity. Functionalization of specific brain regions using ultrasound-sensitive proteins can offer submillimeter spatial precision. Localization of sonogenetic proteins in combination with an acoustic field provided by a diffuser assembly will also ensure that the observed neuromodulatory effects are solely due to ultrasound activation of targeted regions of tissue and not due to the confounding effects of reflection or interference from the geometry of the skull.

4. Experimental Section

Ultrasound Transducers: Ultrasound transducers used in this study were single crystal lithium niobate transducers operating in the thickness mode with lateral dimensions of 5×5 mm and a thickness of 500 μm . The 128YX cut of lithium niobate was used and the fabrication process involved cleaning of the wafer with acetone, isopropyl alcohol, and

ultrapure deionized (DI) water followed by sputtering both sides with an adhesion layer of 20 nm titanium followed by 1 μm gold. The deposition parameters were (with a Denton Discovery 635, Denton Vacuum LLC, NJ, USA) 5–10 nm of Ti at $1.2\text{--}1.6 \text{ \AA s}^{-1}$ with the power set to 200 W, with argon as the gas in the chamber at 2.3 mT and the stage rotating at 13 RPM to ensure uniform deposition over the sample. The thickness of gold deposited was 1 μm at a rate of $7\text{--}9 \text{ \AA s}^{-1}$.

Diffuser Fabrication and Characterization: Code (MATLAB, Mathworks, MA, USA) was used to define the well depths based on the medium of choice and was used to define a computer-aided design program that controlled the laser machining operation. The excimer machining laser used for this application was a 6 mJ, 200 Hz, 248 nm (Lasershot, Optec Inc., San Diego, CA, USA and Frameries, Belgium) KrF laser machining system. A grid was defined using the method of quadratic residues described above and the well depth was calculated for each increment along the X and Y directions. The parameters needed for determining well depth are the speed of sound in glass, $c = 4550 \text{ m s}^{-1}$, and the operating frequency of the transducer, $\omega_r = 2\pi f$, where f in this case is 7 MHz, corresponding to the fundamental frequency for 500 μm -thick 128YX lithium niobate.^[38] The well depth ranged up to 309 μm and required between three and ten laser machining passes. The machined diffuser was bonded to the transducer face using a UV-curable epoxy (NOA81, Norland Products Inc., Cranbury, NJ, USA) using previously described techniques.^[50] This fabrication technique enables the miniaturization of devices that are capable of producing diffuse acoustic fields irrespective of the nature of the enclosed volume, as determined using surface and domain measurements as follows. A scanning laser Doppler vibrometer (UHF-120SV, Polytec, Waldbronn, Germany) was used to characterize the displacement of the substrate when actuated. Measurements of the pressure output from the transducer were performed using a fiber optic hydrophone (FOHS92, Precision Acoustics, Dorchester, UK).

Ultrasound Field Simulation: Finite element analysis (COMSOL 5.5, Comsol Inc., Los Angeles, CA, USA) was used to simulate the system as a linear media with a time-dependent acoustic pressure field present in two dimensions. The boundaries between the coupling fluid and the coverslip, and the coverslip and the media above it were defined as

acoustic–structure boundaries, where there is fluid load on the structure due to pressure waves originating from the ultrasound source and structural acceleration on the fluid domain across the fluid–solid boundary. This results in stress build-up in the coverslip that is translated to the fluid domain above it for the duration of the stimulation. The coverslip was defined to have the elastic properties of silica glass, with an isotropic Young's modulus of 73.1 GPa, a density of 2203 kg m⁻³ and a Poisson's ratio of 0.17. The distance between the transducer and the upper boundary is 5 mm. The simulations were conducted in the time domain, with a 20 μs burst followed by a 30 μs dwell to observe changes in the pressure field both during and after the stimulus. The acoustic field was modeled as a sinusoidal input to the transducer, $d = 5 \sin(\omega t)$ nm, and the fluid domain was defined to have the properties of water ($\rho = 1000 \text{ kg m}^3$, $c = 1500 \text{ m s}^{-1}$). The maximum mesh size was chosen so that all element sizes were always less than one-eighth of a wavelength, and the data were exported every 0.05 μs so that a frequency range of up to 10 MHz could be analyzed. The coverslip was defined to be 500 μm thick and spanned the entire width of the domain. The spatial step chosen for plotting the isofrequency contours was less than $k_{\text{max}} = \omega c^{-1}$.

Imaging Rig for Ultrasound Stimulation: An upright epi-fluorescent microscope (Imager M2, Carl Zeiss GmbH, Gottingen, Germany) was used for the in vitro experiments. For this application we used our transducer assembly placed in a heated stage fixture set to 37 °C underneath the cell chamber, which ensures homeostasis. Stimulus frequency and duration were controlled by a waveform generator (33600A Series, Keysight, CA, USA), and the pressure was controlled through a 300 W amplifier (VTC2057574, Vox Technologies, Richardson, TX, USA). Simultaneous calcium imaging was performed using a 40× water dipping objective at 16.6 frames per second with a camera (Orca Flash 4.0, Hamamatsu Photonics K.K., Japan) and a GFP filter.

HEK293 Cell Culture and Transfection: HEK293 cells (ATCC CRL-1573) were cultured using a standard procedure in DMEM supplemented with 10% fetal bovine serum (FBS) and 20 mM glutamine in a 37 °C and 5% CO₂ incubator. Cells beyond passage 30 were discarded and a new aliquot was thawed. A stable calcium reporter line was generated with a GCaMP6f lentivirus (Cellomics Technology PLV-10181-50) followed by fluorescence-activated cell sorting (FACS). For diffuser experiments, GCaMP6f-expressing HEK cells were seeded on a 12-well cell culture plates with 18 mm glass coverslips coated with poly-D-lysine (PDL) (10 μg μL⁻¹; P6407, Sigma-Aldrich, St. Louis, MO, USA) for 1–2 h. Coverslips were washed with (Milli-Q) ultrapure water and cells were seeded at a density of 250 000 cells per well. Cells were transfected with lipofectamine LTX Reagent (15338100, ThermoFisher Scientific, MA, USA) according to the manufacturer's protocol and 24 h after plating, using 500 ng DNA of the clone of interest for each well. Cells were kept at 37 °C for an additional 24 h before imaging on our ultrasound stimulation setup. For imaging, coverslips were mounted on a specialized chamber featuring an ultrasound transducer approximately 5 mm below the coverslip and a 10 mL reservoir of media above the coverslip. Once cells were in focus, an ultrasound pulse of 100 ms duration was delivered as described in previous sections while imaging with a 40× immersion objective, and a cell membrane profile was reconstructed and analyzed from these images (ImageJ, National Institutes of Health, Bethesda, MD, USA).

Calcium Imaging: Calcium imaging analysis was performed using custom scripts written as ImageJ macros. Transfected cells were segmented and cell fluorescence over time in the GCaMP6f channel was measured and stored in comma-delimited text (csv) files. Calcium data were analyzed using custom Python scripts. Calcium signals were normalized as $\Delta F/F$ using a 6 s baseline for each region of interest (ROI) and a peak detection algorithm with a fixed threshold of 0.25 was used to identify responsive cells after ultrasound stimulation.

Ex Vivo Hydrophone Measurements in Murine Model and Animal Safety Considerations: Hydrophone measurements were performed with a fiber-optic hydrophone (FOHS92, Precision Acoustics, Dorchester, UK) ex vivo. C57BL/6 mice (JAX 000664), aged 10–14 weeks, were sacrificed and decapitated. The skin over the skull was removed, followed by removal of

the lower mandible, soft palate, and hard palate. Once the ventral part of the brain was exposed, the mouse head preparation was placed dorsal side down on the diffuser assembly coupled with ultrasound gel, and the hydrophone tip was lowered into the ventral portion of the brain using a micromanipulator (Figure S3, Supporting Information).

This study was performed using one adult mouse, conforming to ARRIVE guidelines 2.0 (National Centre for the Replacement, Refinement & Reduction of Animals in Research). The work was conducted by A. Vasan and U. Magaram in the Salk Institute in La Jolla, CA. A. Vasan was present for all hydrophone measurements. No control mice were used. The mouse was randomly and blindly selected from 20 healthy mice. No exclusions were made. Animals used in this trial were group housed in an American Association for the Accreditation of Laboratory Animal Care approved vivarium on a 12 h light/dark cycle, and all protocols were approved by the Institutional Animal Care and Use Committee of the Salk Institute for Biological Studies (protocol # 15–00064). Food and water were provided ad libitum, and nesting material was provided as enrichment. The mouse was euthanized using CO₂ according to approved protocols before decapitation and dissection for the hydrophone measurements.

A murine model was selected for this study for the following reasons: 1) Mice to be used in this study represent a published model for sonogenetics. 2) From an anatomical and physiological perspective, the mouse brain is an acceptable approximation of the human brain. This is important because the test system that is being used in this study is one that may find its way into human use in the future. 3) Historically, the mouse has proved to be an excellent model for neurological evaluations and therapy in humans. 4) The experience of the laboratory with this model produces better judgment concerning model-related complications. 5) Artificial (in silico) and computational models are inadequate to represent the complexity of the neurological system in mice (and humans) in understanding sonogenetics. 6) Smaller animals lack the scale and complexity of the surrounding skull necessary for sufficient evaluation of the technology considered in this study.

Supporting Information

Supporting Information is available from the Wiley Online Library or from the author.

Acknowledgements

The authors are grateful to the University of California San Diego for provision of funds and facilities in support of this work. J.F. is grateful for funding for this work from the W.M. Keck Foundation via a SERF grant and, with S.C., from the National Institutes of Health via R01NS115591. S.C. is also grateful to the NIH in support of this work via grant R01MH MH111534. This work was performed at the Medically Advanced Devices Laboratory at the University of California, San Diego and the Chalasani lab at the Salk Institute of Biological Sciences. Fabrication was performed in part at the San Diego Nanotechnology Infrastructure (SDNI) of UCSD, a member of the National Nanotechnology Coordinated Infrastructure, which is supported by the National Science Foundation (Grant ECCS–1542148). The authors are grateful to John Roy and team in San Diego from Optec Laser Systems for substantial training, assistance, and advice in laser machining throughout this effort. The authors would like to thank members of the Medically Advanced Devices Laboratory and the Chalasani Laboratory for feedback on this manuscript.

Conflict of Interest

The authors declare no conflict of interest.

Author Contributions

J.F. and A.V.: designed the research; A.V.: built, characterized the devices and conducted experiments; A.V., F.A., and N.B.: analyzed data; M.D.: performed in-vitro studies; S.H.C. supervised the research at the Salk Institute; A.V. and U.M.: performed the ex-vivo study. A.V. and J.F. wrote the paper.

Data Availability Statement

The data that support the findings of this study are available from the corresponding author upon reasonable request.

Keywords

acoustofluidics, architectural acoustics, neuromodulation, sonogenetics, ultrasound

Received: October 19, 2021

Revised: January 18, 2022

Published online:

-
- [1] M. R. Schroeder, *J. Acoust. Soc. Am.* **1979**, *65*, 958.
 [2] M. R. Schröder, *J. Acoust. Soc. Am.* **1975**, *57*, 149.
 [3] Y. Zhu, X. Fan, B. Liang, J. Cheng, Y. Jing, *Phys. Rev. X* **2017**, *7*, 021034.
 [4] J. Huang, P. E. Dupont, A. Undurti, J. K. Tiedman, R. O. Cleveland, *Ultrasound Med. Biol.* **2006**, *32*, 721.
 [5] J. Behrens, S. Langelier, A. R. Rezk, G. Lindner, L. Y. Yeo, J. R. Friend, *Lab Chip* **2015**, *15*, 43.
 [6] K. Melde, A. G. Mark, T. Qiu, P. Fischer, *Nature* **2016**, *537*, 518.
 [7] S. Jiménez-Gambn, N. Jiménez, J. M. Benlloch, F. Camarena, *Phys. Rev. Appl.* **2019**, *12*, 014016.
 [8] P. N. Wells, *Phys. Med. Biol.* **2006**, *51*, R83.
 [9] M. Kinoshita, N. McDannold, F. A. Jolesz, K. Hynynen, *Proc. Natl. Acad. Sci.* **2006**, *103*, 11719.
 [10] D. K. Piech, B. C. Johnson, K. Shen, M. M. Ghanbari, K. Y. Li, R. M. Neely, J. E. Kay, J. M. Carmena, M. M. Maharbiz, R. Muller, *Nat. Biomed. Eng.* **2020**, *4*, 207.
 [11] Y. Tufail, A. Yoshihiro, S. Pati, M. M. Li, W. J. Tyler, *Nat. Protocols* **2011**, *6*, 1453.
 [12] S. Wang, X. Guo, W. Xiu, Y. Liu, L. Ren, H. Xiao, F. Yang, Y. Gao, C. Xu, L. Wang, *Sci. Adv.* **2020**, *6*, 31.
 [13] K. Hynynen, R. M. Jones, *Phys. Med. Biol.* **2016**, *61*, R206.
 [14] G. Li, W. Qiu, Z. Zhang, Q. Jiang, M. Su, R. Cai, Y. Li, F. Cai, Z. Deng, D. Xu, H. Zhang, H. Zheng, *IEEE Trans. Biomed. Eng.* **2019**, *66*, 217.
 [15] J. Song, A. Pulkkinen, Y. Huang, K. Hynynen, *IEEE Trans. Biomed. Eng.* **2011**, *59*, 435.
 [16] R. D. Airan, K. B. Pauly, *Neuron* **2018**, *98*, 875.
 [17] T. Azuma, K.-I. Kawabata, S.-I. Umemura, M. Ogihara, J. Kubota, A. Sasaki, H. Furuhashi, *Jpn. J. Appl. Phys.* **2005**, *44*, 4625.
 [18] M. Daffertshofer, A. Gass, P. Ringleb, M. Sitzer, U. Sliwka, T. Els, O. Sedlaczek, W. J. Koroshetz, M. G. Hennerici, *Stroke* **2005**, *36*, 1441.
 [19] C. Baron, J.-F. Aubry, M. Tanter, S. Meairs, M. Fink, *Ultrasound Med. Biol.* **2009**, *35*, 1148.
 [20] M. Morozov, D. Damjanovic, N. Setter, *J. Eur. Ceram. Soc.* **2005**, *25*, 2483.
 [21] S. Ibsen, A. Tong, C. Schutt, S. Esener, S. H. Chalasani, *Nat. Commun.* **2015**, *6*, 8264.
 [22] M. Duque, C. A. Lee-Kubli, Y. Tufail, U. Magaram, J. M. Lopez, E. Edsinger, A. Vasani, R. Shiao, C. Weiss, J. Friend, S. H. Chalasani, *bioRxiv* **2020**.
 [23] R. C. Challis, S. Ravindra Kumar, K. Y. Chan, C. Challis, K. Beadle, M. J. Jang, H. M. Kim, P. S. Rajendran, J. D. Tompkins, K. Shivkumar, B. E. Deverman, V. Gradinaru, *Nat. Protocols* **2019**, *14*, 379.
 [24] J. O. Szablowski, A. Bar-Zion, M. G. Shapiro, *Acc. Chem. Res.* **2019**, *52*, 2427.
 [25] A. Vasani, J. Orosco, U. Magaram, M. Duque, C. Weiss, Y. Tufail, S. H. Chalasani, J. Friend, *Adv. Sci.* **2021**, *9*, 1.
 [26] K. Reinhold, A. D. Lien, M. Scanziani, *Nat. Neurosci.* **2015**, *18*, 1789.
 [27] K. K. Sellers, D. V. Bennett, A. Hutt, J. H. Williams, F. Fröhlich, *J. Neurophysiol.* **2015**, *113*, 3798.
 [28] P. Muralt, N. Ledermann, J. Paborowski, A. Barzegar, S. Gentil, B. Belgacem, S. Petitgrand, A. Bosseboeuf, N. Setter, *IEEE Trans. Ultrason. Ferroelectr. Freq. Control* **2005**, *52*, 2276.
 [29] Y. Hou, J.-S. Kim, S. Ashkenazi, S.-W. Huang, L. J. Guo, M. O'Donnell, *Appl. Phys. Lett.* **2007**, *91*, 073507.
 [30] D. R. Namjoshi, W. H. Cheng, K. A. McInnes, K. M. Martens, M. Carr, A. Wilkinson, J. Fan, J. Robert, A. Hayat, P. A. Crompton, C. L. Wellington, *Mol. Neurodegener.* **2014**, *9*, 55.
 [31] H. Wang, Y. Ma, H. Yang, H. Jiang, Y. Ding, H. Xie, *Micromachines* **2020**, *11*, 928.
 [32] A. Kawamata, H. Hosaka, T. Morita, *Sens. Actuators A Phys.* **2007**, *135*, 782.
 [33] R. Turyn, *IEEE Trans. Inf. Theory* **1967**, *13*, 524.
 [34] H. Kuttruff, *Appl. Acoust.* **1994**, *42*, 215.
 [35] R. L. King, J. R. Brown, W. T. Newsome, K. B. Pauly, *Ultrasound Med. Biol.* **2013**, *39*, 312.
 [36] R. J. Wood, *Am. Sci.* **2014**, *102*, 124.
 [37] P. Morris, A. Hurrell, A. Shaw, E. Zhang, P. Beard, *J. Acoust. Soc. Am.* **2009**, *125*, 3611.
 [38] S. Collignon, O. Manor, J. Friend, *Adv. Funct. Mater.* **2018**, *28*, 1704359.
 [39] T.-W. Chen, T. J. Wardill, Y. Sun, S. R. Pulver, S. L. Renninger, A. Baohan, E. R. Schreier, R. A. Kerr, M. B. Orger, V. Jayaraman, L. L. Looger, K. Svoboda, D. S. Kim, *Nature* **2013**, *499*, 295.
 [40] D. P. Darrow, *Neurotherapeutics* **2019**, *16*, 88.
 [41] J. Ye, S. Tang, L. Meng, X. Li, X. Wen, S. Chen, L. Niu, X. Li, W. Qiu, H. Hu, M. Jiang, S. Shang, Q. Shu, H. Zheng, S. Duan, Y. Li, *Nano Lett.* **2018**, *18*, 4148.
 [42] J. Kubanek, J. Shi, J. Marsh, D. Chen, C. Deng, J. Cui, *Sci. Rep.* **2016**, *6*, 1.
 [43] Z. Qiu, J. Guo, S. Kala, J. Zhu, Q. Xian, W. Qiu, G. Li, T. Zhu, L. Meng, R. Zhang, H. C. Chan, H. Zheng, L. Sun, *iScience* **2019**, *21*, 448.
 [44] S. Yoo, D. R. Mittelstein, R. C. Hurt, J. J. Lacroix, M. G. Shapiro, *bioRxiv* **2020**.
 [45] L. A. Gimeno, E. Martin, O. Wright, B. E. Treeby, in *2019 IEEE International Ultrasonics Symposium (IUS)*. IEEE, Piscataway, NJ **2019**, pp. 556–559.
 [46] C. C. Church, C. Labuda, K. Nightingale, *Ultrasound Med. Biol.* **2015**, *41*, 472.
 [47] American Institute of Ultrasound in Medicine, Statement on mammalian biological effects in tissues without gas bodies, **2015**.
 [48] K. G. Foote, *J. Acoust. Soc. Am.* **2014**, *136*, 1511.
 [49] T. Cox, P. D'Antonio, *Build. Acoust.* **2003**, *10*, 1.
 [50] S. M. Langelier, L. Y. Yeo, J. Friend, *Lab Chip* **2012**, *12*, 2970.